Monthly Notices of the ROYAL ASTRONOMICAL SOCIETY

MNRAS **477,** 1270–1284 (2018) doi:10.1093/mnras/sty647
Advance Access publication 2018 March 15

Circumbinary, not transitional: on the spiral arms, cavity, shadows, fast radial flows, streamers, and horseshoe in the HD 142527 disc

Daniel J. Price,[1★] Nicolás Cuello,[2,3,4] Christophe Pinte,[1,5] Daniel Mentiplay,[1] Simon Casassus,[3,6] Valentin Christiaens,[3,6] Grant M. Kennedy,[7] Jorge Cuadra,[2,3,4] M. Sebastian Perez,[3,6] Sebastian Marino,[7] Philip J. Armitage,[8,9] Alice Zurlo,[3,6] Attila Juhasz,[7] Enrico Ragusa,[10] Guillaume Laibe[11] and Giuseppe Lodato[10]

[1]*Monash Centre for Astrophysics (MoCA) and School of Physics and Astronomy, Monash University, Clayton, Vic 3800, Australia*
[2]*Instituto de Astrofísica, Pontificia Universidad Católica de Chile, Santiago, Chile*
[3]*Instituto de Astrofísica, Pontificia Universidad Católica de Chile, 7820436 Macul, Santiago, Chile*
[4]*Núcleo Milenio de Formación Planetaria (NPF), Chile*
[5]*Univ. Grenoble Alpes, CNRS, IPAG/UMR 5274, F-38000 Grenoble, France*
[6]*Departamento de Astronomía, Universidad de Chile, Casilla 36-D, Santiago, Chile*
[7]*Institute of Astronomy, University of Cambridge, Madingley Rd, Cambridge CB3 0HA, UK*
[8]*JILA, University of Colorado and NIST, 440 UCB, Boulder, CO 80309-0440, USA*
[9]*Department of Astrophysical and Planetary Sciences, University of Colorado, 391 UCB, Boulder, CO 80309-0391, USA*
[10]*Dipartimento di Fisica, Università Degli Studi di Milano, Via Celoria 16, I-20133 Milano, Italy*
[11]*Univ Lyon, Univ Lyon1, Ens de Lyon, CNRS, Centre de Recherche Astrophysique de Lyon UMR5574, F-69230 Saint-Genis-Laval, France*

Accepted 2018 March 6. Received 2018 February 13; in original form 2017 December 22

ABSTRACT

We present 3D hydrodynamical models of the HD 142527 protoplanetary disc, a bright and well-studied disc that shows spirals and shadows in scattered light around a 100 au gas cavity, a large horseshoe dust structure in mm continuum emission, together with mysterious fast radial flows and streamers seen in gas kinematics. By considering several possible orbits consistent with the observed arc, we show that all of the main observational features can be explained by one mechanism – the interaction between the disc and the observed binary companion. We find that the spirals, shadows, and horseshoe are only produced in the correct position angles by a companion on an inclined and eccentric orbit approaching periastron – the 'red' family from Lacour et al. Dust–gas simulations show radial and azimuthal concentration of dust around the cavity, consistent with the observed horseshoe. The success of this model in the HD 142527 disc suggests other mm-bright transition discs showing cavities, spirals, and dust asymmetries may also be explained by the interaction with central companions.

Key words: accretion, accretion discs – planet–disc interactions – protoplanetary discs – binaries: general – submillimetre: planetary systems.

1 INTRODUCTION

Around the young star HD 142527 lies an enigmatic and spectacular protoplanetary disc. Cycle 0 observations with the Atacama Large Millimeter/submillimeter Array (ALMA) by Casassus et al. (2013) revealed a 'horseshoe' of dust continuum emission (first detected by Ohashi 2008) surrounding a ∼90–140 au central cavity (cavities being the defining feature of so-called 'transitional' or 'transition discs'; Strom et al. 1989; Espaillat et al. 2014). The first ALMA observations also revealed diffuse CO gas inside the cavity alongside mysterious 'streamers' or 'filaments' seen in HCO+ emission, thought to indicate flow across a planet-induced gap (Casassus et al. 2013).

The star itself is a Herbig Fe star of spectral type F6 IIIe ($M \approx 1.8\,M_\odot$) at a distance of 156^{+7}_{-6} pc (Gaia Collaboration et al. 2016) in the Sco–Cen association (Biller et al. 2012; Mendigutía et al. 2014). Modelling of the spectral energy distribution (SED) suggested a disc gap between 30 and 130 au (Verhoeff et al. 2011), confirmed by the initial ALMA observations (Casassus et al. 2013). Earlier mid-infrared (IR) observations (van Boekel et al. 2004; Fujiwara et al. 2006) and more recent scattered light images (Avenhaus et al. 2017) found a small inner disc inside the cavity of ∼10 au in radius. The high accretion rate on to the central star ($\approx 2 \times 10^{-7}\,M_\odot\,yr^{-1}$;

★ E-mail: daniel.price@monash.edu

Garcia Lopez et al. 2006; Mendigutía et al. 2014) implies that the small inner disc must be refilled from the outer disc, most likely in an episodic manner (Casassus et al. 2013).

Even before ALMA, the disc around HD 142527 had proved spectacular, with a spiral arm detected at $R \gtrsim 100$ au in scattered light observations in the near-IR by Fukagawa et al. (2006). Further observations revealed a wealth of spiral structure, including small near-IR spirals at the edge of the cavity (Casassus et al. 2012; Canovas et al. 2013; Avenhaus et al. 2014, 2017), a counterpart to the Fukagawa et al. (2006) spiral seen in the CO emission in further ALMA observations, and two further large-scale (∼500 au) spiral arms by Christiaens et al. (2014).

Fukagawa et al. (2006) first suggested that the spirals might be caused by an inner companion, with the presence of a 0.1–0.4 $M_\odot$ companion with a projected separation of ∼13 au confirmed by Biller et al. (2012) using Sparse Aperture Masking (SAM) with the NACO instrument on the Very Large Telescope (VLT). More recent observations have refined both the orbit and the companion mass (Close et al. 2014; Lacour et al. 2016, hereafter L16).

Scattered light images also revealed shadows cast across the outer disc (Fukagawa et al. 2006; Avenhaus et al. 2014). Marino, Perez & Casassus (2015a) satisfyingly reproduced the observed illumination pattern by assuming a compact ∼10 au inclined and thin inner disc casting shadows on the outer disc, with a relative inclination of ∼70°. This is consistent with the estimated inclination of the inner binary with respect to the disc (L16).

Perhaps the greatest surprise were the complexities found in detailed kinematic studies using CO(6–5) molecular line data by Casassus et al. (2015a), with evidence for a warped disc and near free-fall motions within the central cavity, suggested to be related to theoretical models of 'disc tearing' in warped accretion discs (Nixon, King & Price 2013; Nealon, Price & Nixon 2015).

Understanding the origin of features in the HD 142527 disc is important because several of these appear common to a broad class of discs. In particular, dust horseshoes or rings surrounding the central cavities in mm-bright transition discs appear to be widespread (Canovas et al. 2016; van der Marel et al. 2016; see review by Casassus 2016), with horseshoes normally interpreted as 'dust traps' caused by a vortex at the edge of a planet-induced gap (e.g. Pinilla et al. 2012; van der Marel et al. 2013; Marino et al. 2015b; Baruteau & Zhu 2016). Spirals are also observed in an increasing number of discs (Garufi et al. 2013; Benisty et al. 2015, 2017; Pérez et al. 2016). Thus, unlocking the mystery of HD 142527 may help to shed light on the origin of these features in this wider class of discs.

Our approach is to perform 3D hydrodynamical and dust–gas simulations of the disc–binary interaction, to try to explain the observed features in the HD 142527 disc. We describe the key observations in Section 2, methods and initial conditions in Section 3. Results are in Section 4. We discuss in Section 5 and summarize in Section 6.

2 OBSERVATIONAL CONSTRAINTS

The sheer volume of data collected on HD 142527 provides tight constraints on theoretical models, and it seems optimistic to assume that a single model could explain multiple observed features simultaneously. From a dynamical perspective the main puzzles are as follows.

(i) *Shadows*. The close agreement found by Marino et al. (2015a) between their radiative transfer model and the scattered light images means these shadows are almost certainly cast by an inner circumprimary disc inclined to the outer disc plane by ∼70°. The size of such a disc would be consistent with the IR observations (Verhoeff et al. 2011). The constraints from ALMA CO observations of the inner disc suggest that it is small and with unusual (non-Keplerian) kinematics between the inner and outer disc (Casassus et al. 2015a; Perez et al. 2015).

(ii) *Fast radial flows*. Casassus et al. (2015a) suggested an explanation for fast radial flows in terms of disc tearing by an inclined inner binary (e.g. Nixon et al. 2013). However, subsequent simulations by Dunhill and collaborators (reported in Cuadra 2016) found that such a binary tended to simply break the disc into two distinct sections, as found by Facchini, Lodato & Price (2013) and consistent with expectations of warp dynamics in thick ($H/R \sim 0.1$) protoplanetary discs. Rosenfeld, Chiang & Andrews (2014) also found that the fast radial flows were better explained by free-fall radial velocities rather than a warp, suggesting material is somehow able to shed angular momentum and plunge into the central regions. Those authors proposed gravitational torques from giant planets or brown dwarfs as a possible solution.

(iii) *Spiral arms*. Spirals are seen immediately outside the cavity in both scattered light (Fukagawa et al. 2006; Avenhaus et al. 2014, 2017; Rodigas et al. 2014) and in CO emission (Christiaens et al. 2014). These are usually attributed to the presence of either companions orbiting interior or exterior to the arms (Dong et al. 2015), to a gravitationally unstable disc (Dipierro et al. 2015a), or to some combination of both (Pohl et al. 2015). Quillen (2006) offered an explanation of similar spirals seen in the disc around HD 100546 in terms of a precessing, warped disc driven by misaligned embedded protoplanets. Montesinos et al. (2016) also showed that spiral structure could be induced by temperature fluctuations caused by shadows.

(iv) *Cavity*. The origin of central cavities in transitional discs is not yet certain (Williams & Cieza 2011). Traditionally central holes were thought to arise from either photoevaporation of gas by the central star or depletion of gas and/or dust due to formation of planetary mass companions (Andrews et al. 2011; Williams & Cieza 2011; Espaillat et al. 2014; Owen 2016). Zhu et al. (2012) found that dust filtering by giant planets (e.g. Rice et al. 2006) could partially explain the mm-dust holes seen in many transition discs, but that the depletion in small particles was insufficient to explain the near-IR deficit in the SED. An alternative possibility is the tidal truncation of the disc from a central binary (Artymowicz & Lubow 1994). While a low-mass companion has been found in HD 142527 (see below), previous authors (e.g. L16) have assumed that the projected orbital separation of ∼13 au is too small to tidally truncate the disc out to 100 au – the size of the observed CO cavity (Muto et al. 2015; Perez et al. 2015; Boehler et al. 2017).

(v) *Dust horseshoe*. Currently the main accepted model for producing dust horseshoes in mm-bright transition discs involves dust trapping by a gap-edge vortex (Pinilla et al. 2012; Lyra & Lin 2013). Ataiee et al. (2013) considered an alternative model where dust horseshoes could be produced by eccentric circumbinary cavities, but dismissed this model based on their simulations. However, dust evolution was added only in post-processing that neglects the role of tidal torques on the dust and backreaction, leading to potentially misleading conclusions. Recently, Ragusa et al. (2017) showed that central binaries can produce both rings and horseshoes in dust emission. Indeed, eccentricities around the cavity edge are a common feature in hydrodynamical simulations of circumbinary discs (Kley & Dirksen 2006; Farris et al. 2014; Ragusa, Lodato & Price 2016). Ragusa et al. (2017) showed that more massive companions produce progressively more asymmetric structures,

with simulated ALMA observations closely matching observed discs.

(vi) *Gap-crossing filaments*. Casassus et al. (2013) attributed these to flows of gas through a planetary gap, as observed commonly in simulations of gap opening by embedded planets in discs (e.g. Bryden et al. 1999; Lubow & D'Angelo 2006). However, it is not clear how the 'filaments' might be obviously related to either the companion or any other putative planets, nor how they relate to the fast radial flows, or whether they may be illumination effects due to shadowing from the tilted inner disc.

A clue to solving the puzzle is that all of the above features may in principle be caused by the interaction with an (inclined) central binary (Fukagawa et al. 2006). The main issue is how a binary with a $\sim$13 au projected separation could carve a $\sim$90–140 au cavity. This led L16 to conclude that the cavity could not be created by the binary. However, the orbit is poorly constrained, with best-fitting orbits from L16 suggesting significant eccentricity.

3 NUMERICAL METHODS

We perform 3D hydrodynamics simulations of the disc–binary interaction using the PHANTOM smoothed particle hydrodynamics (SPH) code (Price et al. 2018; for reviews of SPH see Monaghan 2005; Price 2012). We also perform several models with dust and gas to see if we can simultaneously produce the dust horseshoe. Our approach to dust–gas modelling is similar to that used in our previous papers (Dipierro et al. 2015b, 2016), where we model the dust using a separate set of particles coupled to the gas via a drag term (Laibe & Price 2012a,b; Price et al. 2018).

3.1 Initial conditions

3.1.1 Binary

We model the binary using sink particles that interact with the gas disc only via gravity and by accreting gas (Bate, Bonnell & Price 1995). The sink particles are free to migrate and also change mass and orbital parameters due to interaction with the gas disc. We set the primary mass to 1.8 $M_\odot$ (from the spectral type), and constrained by the total mass estimate of $\sim 2.1 \pm 0.2\,M_\odot$ from the Keplerian motion of the outer disc (Casassus et al. 2015a) we set the companion mass to 0.4 $M_\odot$ (the latest observational estimates based on spectral fitting are in the range 0.2–0.4 $M_\odot$; Christiaens et al. 2018). Since our chosen mass of 0.4 $M_\odot$ is at the higher end of this range, we also performed an additional set of calculations employing lower mass companions. We found that our results are not strongly sensitive to the secondary mass, with companion masses as low as 0.1 $M_\odot$ producing the same cavity but with lower amplitude perturbations around the cavity edge. The change in mass due to accretion is negligible in our simulations.

We fix the accretion radii for both sinks to 1 au in order to resolve the circumprimary disc, if present.

3.1.2 Binary orbit

After a few trial simulations with binaries of various semimajor axes and eccentricities, and from previous attempts at modelling HD 142527 (see Cuadra 2016), we realized the importance of the known observational constraints on the orbit. To this end we employed IMORBEL[1] to fit the orbit, written by Tim Pearce and Grant Kennedy (Pearce, Wyatt & Kennedy 2015). The same code was also used in L16.

Table 1. Orbital elements for HD 142527B for six trial orbits, drawn from fits to the observed arc with IMORBEL. From left to right: semimajor axis (a, au), eccentricity (e), inclination (i,°), position angle (PA) of ascending node (Ω,°; east of north), argument of pericentre (ω,°), true anomaly (f,°), orbital period (P, yr), and relative angle between disc and binary (θ,°).

Orbit	a	e	i	Ω	ω	f	P	θ
B1	26.5	0.24	119.9	349.7	218.0	25.93	91.8	40.4
B2	28.8	0.40	120.4	340.3	201.5	33.78	104	39.6
B3	34.3	0.50	119.3	159.2	19.98	35.04	135	80.7
R1	31.4	0.74	131.3	44.95	27.88	249.3	118	43.1
R2	38.9	0.61	120.3	19.25	354.0	268.3	164	45.3
R3	51.3	0.70	119.3	201.4	173.3	270.4	247	76.3

Rather than taking the orbital fits directly from L16, we produced a revised set of orbital fits using the *Gaia* distance measurement and with our assumed primary and secondary masses. IMORBEL produces a plot similar to the one shown in fig. 5 of L16, from which one may interactively select orbits with given parameters that match the observational constraints. Our guiding wisdom in selecting trial orbits was (i) to examine orbits similar to the 'blue' and 'red' orbit families found in the Monte Carlo fitting shown in fig. 6 of L16, and (ii) to ensure an apoastron separation for the binary large enough to plausibly explain the cavity size.

Table 1 lists the orbital elements used for the six representative orbits shown in this paper, with the resultant orbits shown in Fig. 1. For clarity we show three representative 'blue' orbits (B1, B2, B3) and three 'red' orbits (R1, R2, R3) listed in order of increasing semimajor axis. The most tightly constrained parameter is the inclination, which is $i = 120^\circ$ for all but one of the orbits. We choose eccentricities ranging from 0.24 to 0.7. The two classes of orbits are 'families' only in a projected sense, as the values of Ω and ω (and hence the orientation perpendicular to the sky plane) change dramatically. The main similarity between each family is simply the location of the periastron in position angle (PA) on the sky and thus whether the binary is approaching (red) or receding (blue) from periastron. The last column in Table 1 gives the angle between the disc and binary angular momentum vectors.

The Monte Carlo fitting performed by L16 found semimajor axes $11 < a < 40$ au, eccentricities $e = 0.5 \pm 0.2$, and inclinations $125^\circ \pm 15^\circ$ to within 1σ probability. Thus all our chosen orbits except R3 fall are probable to within 1σ of these constraints.

Finally, we adopted slightly different conventions for the orbital elements to those used in Pearce et al. (2015) and L16. In particular, we removed the assumption by Pearce et al. (2015) that the angle between the binary and the sky is restricted to be less than 180° (thus flipping the observer from $+z$ to $-z$ depending on the orbit). Since the absolute orientation of the disc and binary is irrelevant in SPH, for convenience we defined the observer to be viewing the disc down the z-axis (i.e. from $z = \infty$). That is, we tilted both the disc and binary in our initial set-up. This simplified our analysis since replicating the observers view of HD 142527 simply meant making an x–y plot in our computational coordinates. Finally, we adapted the set-up routine in PHANTOM to use orbital elements from IMORBEL in the form given in Table 1, such that the public codes are mutually compatible.

[1] http://github.com/drgmk/imorbel

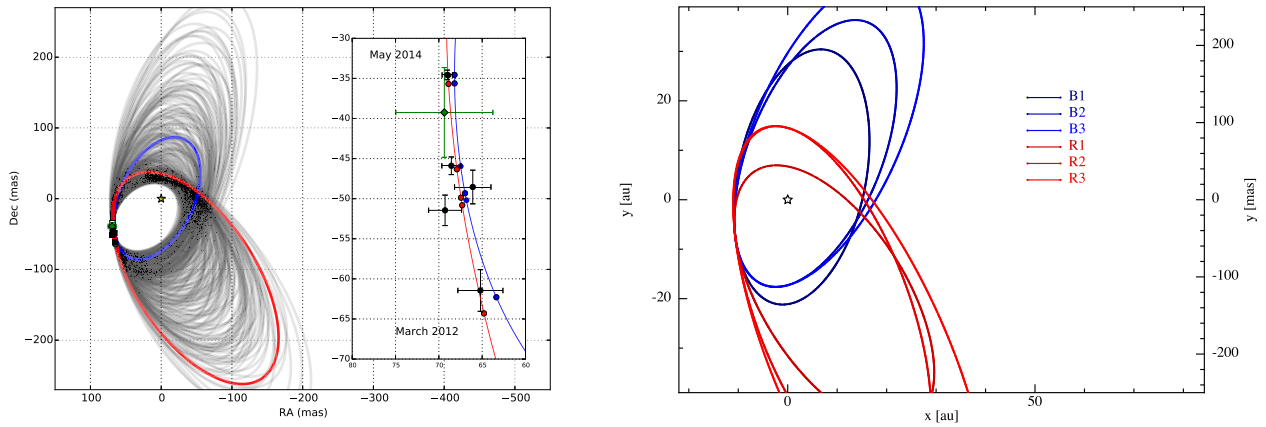

Figure 1. *Binary orbit*. Left: orbital fits for HD 142527B (credit: Lacour et al. 2016, reproduced with permission ©ESO). Right: selected trial orbits for HD 142527B used in this paper, corresponding to the orbital elements listed in Table 1. We assume the *Gaia* distance of 156 pc. The star gives the location of the primary. Motion is clockwise.

3.1.3 Circumbinary disc

We performed two sets of calculations, both with a $0.01\,M_\odot$ circumbinary gas disc but with inner radius set initially to either 50 or 90 au. The $R_{\rm in} = 50$ au calculations ensure that clearing of the inner regions is entirely due to tidal effects, while starting with $R_{\rm in} = 90$ au avoids transient formation of circumprimary and circumsecondary discs. We set the outer radius to $R_{\rm out} = 350$ au (purely for computational efficiency; the real disc extends to ∼600 au). We assume an initially power-law surface density profile $\Sigma \propto R^{-1}$ and model the disc with 10^6 SPH particles assuming a total gas mass of $0.01\,M_\odot$ – see Price et al. (2018) for details of the disc set-up used in PHANTOM. We adopt a mean Shakura–Sunyaev disc viscosity $\alpha_{\rm SS} \approx 0.005$ by setting a fixed artificial viscosity parameter $\alpha_{\rm AV} = 0.25$ in the code and using the 'disc viscosity' flag (see Lodato & Price 2010). Since the artificial viscosity is explicitly specified in SPH, the value of $\alpha_{\rm SS}$ is directly related to $\alpha_{\rm AV}$ according to

$$\alpha_{\rm SS} = \frac{1}{10}\alpha_{\rm AV}\frac{\langle h\rangle}{H}, \qquad (1)$$

where the ratio $\langle h\rangle$ is the mean resolution length at a given radius and H is the disc scale height. There are no additional sources of numerical diffusion in SPH (see Lodato & Price 2010 for detailed calibration and tests). For our chosen resolution the mean h/H in the outer disc is 0.2 (i.e. 5 resolution lengths per scale height), hence the values of $\alpha_{\rm SS}$ and $\alpha_{\rm AV}$ given above.

We prescribe temperature as a function of (spherical) radius according to $T = 28\,{\rm K}(r/r_{\rm in})^{-0.3}$, consistent with the disc model fit by Casassus et al. (2015a) to the observational temperature profile (we use spherical rather than cylindrical radius to avoid confusion when the disc is warped or inclined; see Lodato & Price 2010). This corresponds to $H/R = 0.066$ at $R = R_{\rm in}$ and $H/R = 0.11$ at $R = R_{\rm out}$. More recent observations (Muto et al. 2015; Boehler et al. 2017) found higher temperatures that may suggest a thicker disc. Further modelling of the temperature changes in the disc due to the companion is beyond the scope of this paper but may be important (Verhoeff et al. 2011).

The disc was oriented by $i = 160^\circ$ with respect to the $z = 0$ plane, rotated about a position angle of -20°. That is, our disc is inclined by 20° to the line of sight but with the disc rotating clockwise on the sky, consistent with e.g. Casassus et al. (2015a).

3.2 Radiative transfer

To perform a direct comparison with observations of HD 142527 we post-processed a subset of our simulations using the Monte Carlo radiative transfer code MCFOST (Pinte et al. 2006, 2009). MCFOST is particularly suited to post-processing data from SPH codes because it uses a Voronoi tessellation where each cell corresponds to the position of an SPH particle. Properties such as density, temperature, and velocity may then be mapped directly from the particles to the radiative transfer grid without interpolation.

To irradiate the disc we used the two sink particles as isotropic sources with stellar spectral models appropriate to their mass. Specifically, we adopt 3-Myr isochrones from Siess, Dufour & Forestini (2000), with $T_{\rm eff} = 4800$ K and a luminosity of $2.7\,L_\odot$ for the primary and $T_{\rm eff} = 3700$ K and $L = 0.22\,L_\odot$ for the secondary. We assume astronomical silicates (Draine 2003), with a grain size distribution ranging from 0.03 μm to 1 mm, and a slope of −3.5. Optical properties are calculated using Mie theory. We then used MCFOST to predict line emission from our gas-only simulations for the isotopologues of carbon monoxide including ^{12}CO, ^{13}CO, and C^{18}O and HCO$^+$. We assume a uniform abundance of 5×10^{-5}, 7×10^{-7}, 2×10^{-7}, and 10^{-9} for ^{12}CO, ^{13}CO, C^{18}O, and HCO$^+$, respectively. We assume the gas is in local thermodynamic equilibrium with $T_{\rm gas} = T_{\rm dust}$. We predicted only the line emission, not the continuum, from our gas-only simulations under the assumption that the dust follows the gas. This is a good assumption for grain sizes $\lesssim$10 μm, but for larger grains this assumption no longer holds (see Section 4.5).

4 RESULTS

4.1 Cavity

Fig. 2 shows the column density view of the six calculations corresponding to the orbits listed in Table 2, shown after 20 binary orbital periods with initial $R_{\rm in} = 50$ au. Transient circumprimary discs are present in all calculations except B1. For both 'blue' and 'red' sets of orbits the cavity size scales with semimajor axis (left to right; Artymowicz & Lubow 1994). Cavity size also increases with eccentricity due to the increased apocentre separation (but decreases with inclination; Miranda & Lai 2015). Comparison with the cavity size seen in scattered light, we can exclude binary orbits with $a \gtrsim 50$ au. That with plausible orbits for the observed binary

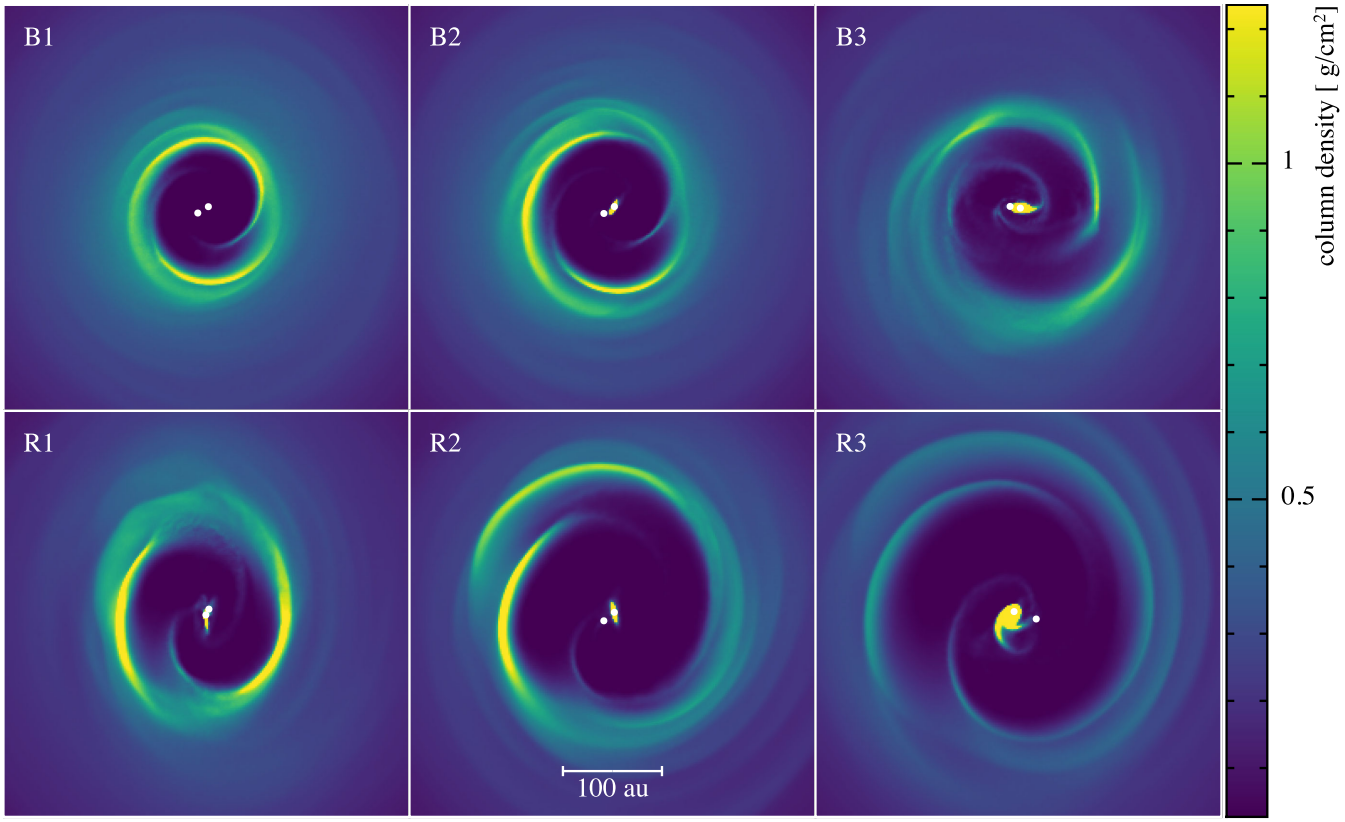

Figure 2. Gas surface densities after 20 orbital periods of the binary for the calculations with $R_{\rm in} = 50$ au, showing the initial dynamical carving of the cavity for binary orbits shown in Fig. 1 and listed in Table 1. Top row shows the 'blue' orbits (binary just past periastron), while bottom row corresponds to the 'red' orbits (binary approaching periastron) from L16. Cavity size scales with apastron separation, with more eccentric binaries (R2, R3) producing cavity sizes consistent with those observed in HD 142527. Transient circumprimary discs are visible in all calculations except B1.

Table 2. Gas mass interior to 90 au (first column); pitch angles along the outer spiral arm at PA of 265° (second column), and within the first and second half of the spiral in PA (third and fourth columns); comparing our simulations to the observations (top row) after 50 orbits of the binary. The final column indicates whether or not the spiral arms show a bifurcation or 'fork' towards the south-west. All simulations obtain residual mass interior to the cavity consistent with the observations. Simulations B3, R2, and R3 show pitch angles most consistent with the data.

	M (<90 au) ($\times 10^{-3}$ M$_\odot$)	Pitch ang. (PA 265°)	Pitch ang. (1st half)	Pitch ang. (2nd half)	SW fork?
Obs	1.7 ± 0.6	4.8°	−3.6°	9.9°	Yes
B1	2.0	1.5°	3.1°	0.0°	No
B2	1.9	1.3°	3.2°	2.5°	No
B3	1.6	5.1°	7.1°	3.2°	No
R1	2.1	−1.8°	−4.0°	0.6°	Yes
R2	1.5	6.0°	6.4°	5.7°	No
R3	1.4	3.6°	6.8°	0.4°	No

we can already produce a cavity size *too big* solves one of the major mysteries of HD 142527 – how a binary with a projected separation of 13 au can produce a 100 au cavity.

Fig. 3 shows the surface density binned as a function of cylindrical radius in the sky plane ($z = 0$). The red dotted line shows the parametrized model adopted by Perez et al. (2015) from fits to the CO emission (specifically, we plot equation 6 from their paper, with parameters taken from their best-fitting model corrected for the *Gaia* distance, giving $R_{\rm cav} = 100$ au). Simulation R2 produces the closest match to the data, with $R_{\rm cav}$ within a few per cent of the observational fit. The remarkable agreement demonstrates that orbits consistent with those inferred by L16 indeed produce cavities of the correct size.

4.2 Gas inside the cavity

The drop in surface density seen in Fig. 3 indicates that the cavity interior is not completely devoid of gas. To quantify this, Table 2 lists the mass interior to 90 au in each of our simulations, compared to the observational measurement from Perez et al. (2015). Regardless of our choice of binary orbit the residual mass inside the cavity agrees with the observational estimate to within the error bars. For example, we measure a residual gas mass of 1.5×10^{-3} M$_\odot$ within 90 au in simulation R2 after 50 orbits, within 11 per cent of the $(1.7 \pm 0.6) \times 10^{-3}$ M$_\odot$ measured by Perez et al. (2015).

Fig. 4 shows the predicted ^{12}CO J = 2–1 emission from simulation R2 (right-hand panel), convolved to a beam size consistent with the Perez et al. (2015) Cycle 0 ALMA data (shown in left-hand panel). We find remarkable agreement with the observed ^{12}CO emission from inside the cavity. In particular there is sufficient gas inside the cavity such that the ^{12}CO is optically thick, as observed. The binary scenario thus naturally explains the residual gas found within the cavity around HD 142527.

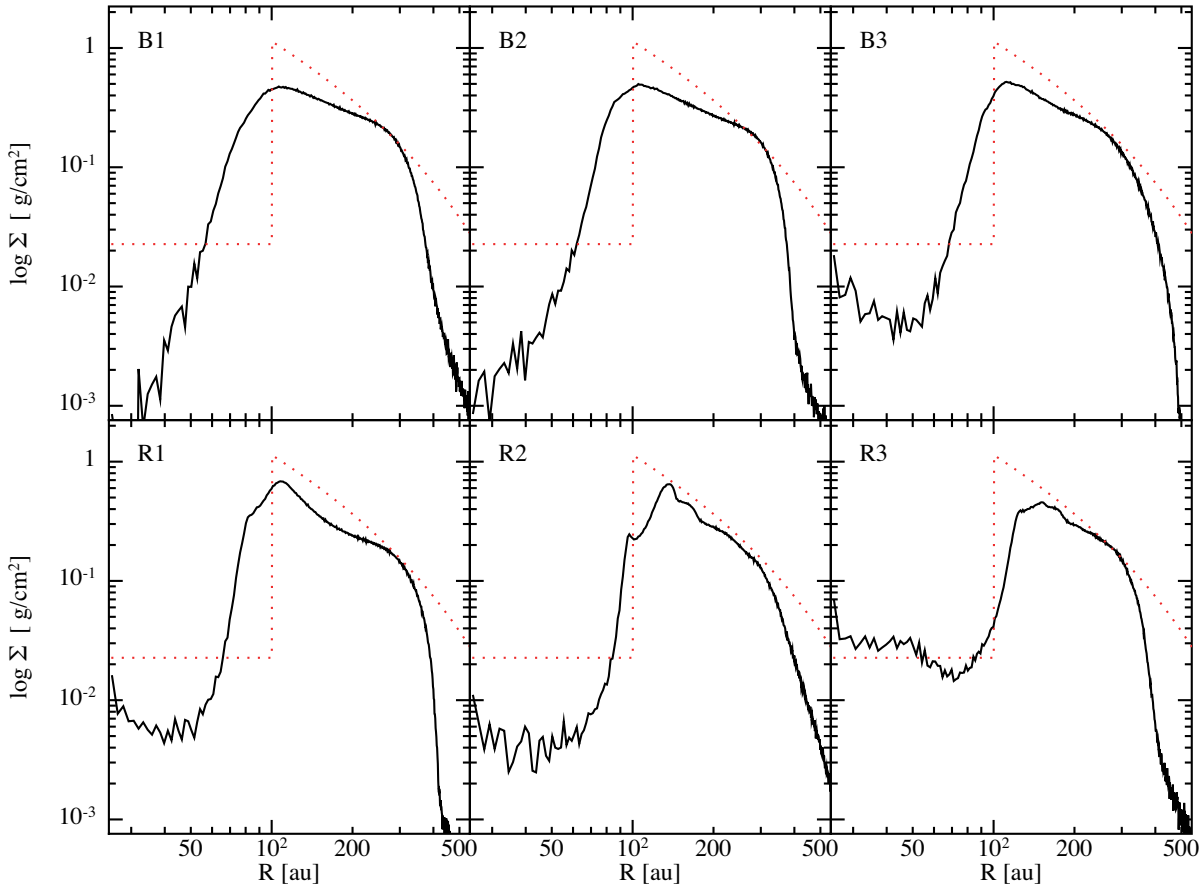

Figure 3. *Cavity*. Surface density as a function of cylindrical radius (in the sky plane) from the $R_{\rm in} = 90$ au calculations after 50 binary orbits. Red dotted line shows the model adopted by Perez et al. (2015) from radiative transfer fitting to CO gas. Simulation R2 shows the closest match to the observed cavity size, with $R_{\rm cav}$ within a few per cent of the gas cavity size inferred from the CO data.

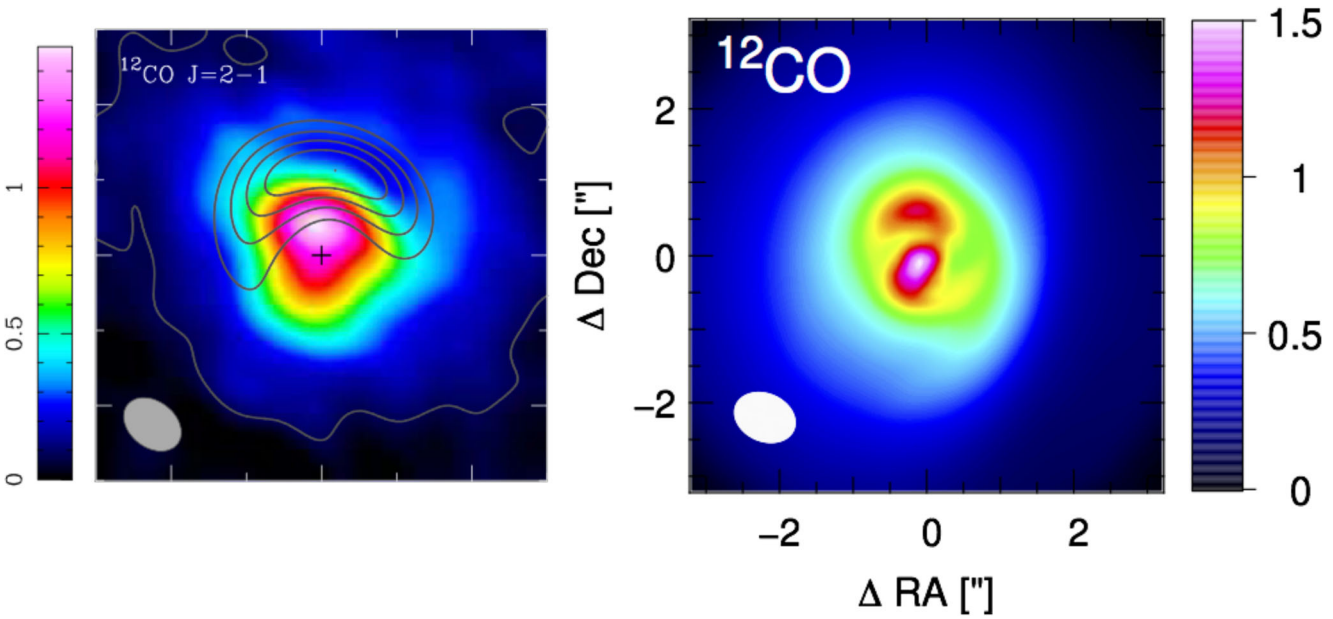

Figure 4. *Gas inside the cavity*. Predicted ^{12}CO J = 2–1 emission from simulation R2 (right), compared to ALMA observations (left; credit: fig. 1 of Perez et al. 2015 ©AAS, reproduced with permission). Sufficient gas remains inside the cavity to produce optically thick ^{12}CO emission, as observed.

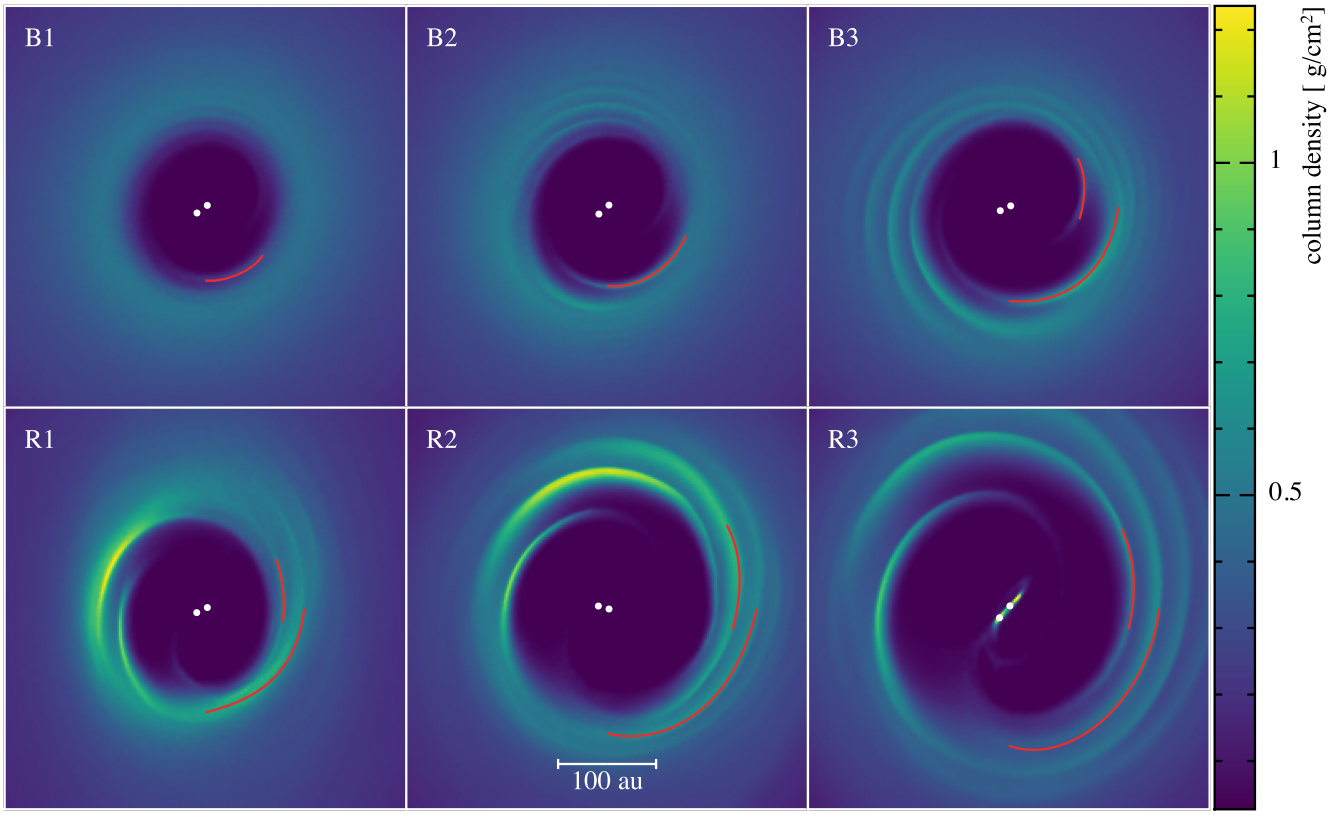

Figure 5. *Spirals*. Gas surface densities after 50 binary orbital periods in calculations with initial $R_{\rm in} = 90$ au, showing the spiral arms. As in Fig. 2, top row shows the 'blue' orbits (binary just past periastron), while bottom row corresponds to the 'red' orbits (binary approaching periastron) from L16. Comparison with the observed spiral structure (left-hand panel of Fig. 6) favours the latter. Comparison with Fig. 2 shows the cavity size is independent of the initial $R_{\rm in}$. Red lines show polynomial fits to 'inner' and 'outer' spiral arms tracing a PA range similar to the scattered light spirals (Fig. 6).

4.3 Spirals

Fig. 5 shows the column density from the $R_{\rm in} = 90$ au calculations after 50 binary orbital periods. In every case three or more prominent spiral arms are seen around the cavity. The companion thus already explains why spiral arms are present around the cavity without needing to invoke gravitational instability or other physics. Comparing the $R_{\rm in} = 50$ au calculations shown in Fig. 2 shows that both calculations produce the same cavity sizes, with the cavity size approximately constant after $\gtrsim$10 orbits of the central binary.

Comparing our results with scattered light (Avenhaus et al. 2014, 2017) and 2-μm (Casassus et al. 2012, 2013) images of HD 142527 shows that the blue orbits (top row) tend to produce spirals inconsistent with the observations. For a more quantitative comparison, we fit the spiral structure with a polynomial of the form $r(\theta) = \sum_{i=0}^{4} a_i \theta^i$. Aside from the formula used to fit the spirals, the fitting procedure is otherwise identical to that described in Christiaens et al. (2014). That is, we trace pixels along the maxima in column density and fit a polynomial to the resulting points using a least-squares fit. Using this procedure we fit 'inner' and 'outer' spiral arms spanning the PA ranges [260°, 305°] and [180°, 270°], respectively, corresponding to the two main spirals seen to the south-west of the cavity in the scattered light image. Red lines in Fig. 5 show the corresponding fits. For orbits B1 and B2 no inner spiral could be fitted, so we only show the outer arm.

Table 2 lists the resulting pitch angles for the outer spiral measured at a PA of 265°, and with the first and second half of the spiral (in PA), corresponding to PA ranges [180°, 225°] (third column) and [225°, 270°] (fourth column). Orbits B1 and B2 in particular show pitch angles too small and little or no asymmetry in the gas distribution around a cavity that is close to circular. Orbit B3 shows promising spirals to the north-east of the cavity, but the spiral arms to the south-west show a series of almost circular tightly wrapped arms not seen in the observations.

The red orbits, by contrast, produce spiral structure and asymmetry in both the cavity and the gas distribution more similar to what is observed (bottom row). In particular, orbit R1 is the only simulation to show a bifurcation in the spiral arms to the south-west of the cavity, as seen in the scattered light image (see Table 2). Orbit R2 is closest to the observed cavity size (Fig. 3) and develops an eccentric cavity similar to those found in previous circumbinary disc simulations (e.g. Farris et al. 2014; D'Orazio et al. 2016; Ragusa et al. 2016) and used by Ragusa et al. (2017) to explain dust horseshoes. The spiral arms appear fixed in relation to the binary orbit, but superimposed on this is an overdensity that rotates at the Keplerian frequency of the outer disc, i.e. on a timescale of 2–3 binary periods (Dunhill, Cuadra & Dougados 2015; Muñoz & Lai 2016). Orbit R3 shows the most open spiral arms (Table 2) but the overdensity around the cavity is less prominent, making it less promising for the observed dust structures. The cavity size is also too big (Fig. 3).

4.4 Shadows

Fig. 2 shows the formation of transient circumprimary discs in the $R_{\rm in} = 50$ au calculations during the first 20 orbits, caused by the

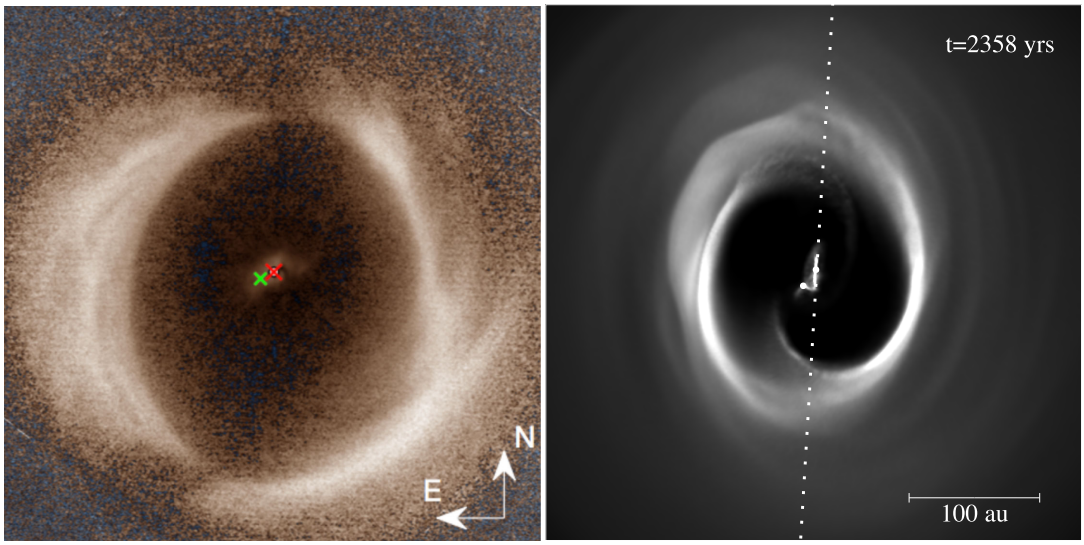

Figure 6. *Shadows*. Column density in the R1 orbit simulated with initial $R_{\rm in} = 50$ au after 20 orbits at the observed orbital phase (right), showing the orientation of the (transient) circumprimary disc, compared to the scattered light (600–900 nm) the Zurich Imaging Polarimeter (ZIMPOL) polarization image (left; taken from fig. 1 of Avenhaus et al. 2017 ©AAS, reproduced with permission). Dotted line indicates the expected shadow from our simulated inner disc (right), which lies close to the orientation of the observed shadows (left).

clearing of the inner disc material. The orientation of these inner discs is highly sensitive to the orbit of the companion. For example, the circumprimary disc in calculation B3 is formed with major axis aligned east–west in our images (i.e. horizontal in Fig. 2), while orbits R1 and R2 produce a disc aligned north–south (i.e. vertical in Fig. 2) – a second piece of evidence favouring the red orbit family. Caution is required, however, since the inner disc precesses with time, though on a time-scale longer than our simulations (∼0.5 Myr; e.g. Owen & Lai 2017). Furthermore, in our $R_{\rm in} = 90$ au calculations we find rotationally supported circumprimary discs only with the R3 orbit at this resolution (Fig. 5; this mainly indicates that the disc mass in other calculations is too low or that the numerical viscosity drains the disc too fast at this resolution; not that circumprimary discs do not exist).

Fig. 6 shows the resultant inner disc structure after 20 orbits (right), shown alongside the scattered light image taken from Avenhaus et al. (2017) (left). Despite the remaining uncertainty in the orbital dynamics the PA of the expected shadow is consistent with the northern shadow seen in the scattered light image, and within 10° of the southern shadow. A difference of 10° is not significant – shadows do not exactly fall in the projected plane of the inner disc due to the vertical extension of the discs (Min et al. 2017). We do not imply that this is the *only* possible orbital configuration that can explain the shadows – nor even the most probable – merely that it is possible to produce a satisfactory orientation of the inner disc to produce the correct shadow from our calculations. We also demonstrate that the orbital dynamics of the companion naturally produces a circumprimary disc with an orientation and size consistent with the structure invoked by Marino et al. (2015a) to explain the observed shadowing.

4.5 Dust horseshoe

Ragusa et al. (2017) found that dust horseshoes similar to those observed by ALMA could be naturally produced by eccentric cavities in gas and dust around binary stars. However, that paper assumed tightly coupled dust grains such that the dust structures merely reflected those in the gas. Whether or not this is the case for the mm continuum emission in HD 142527 (see discussion in Casassus et al. 2015b) depends on the Stokes number – the ratio of the dust stopping time to the disc orbital period.

Assuming subsonic Epstein drag the Stokes number depends only on the gas surface density, according to (Dipierro et al. 2015b)

$$S_{\rm t} = 1 \left(\frac{\Sigma}{0.2\,{\rm g\,cm^{-2}}} \right)^{-1} \left(\frac{\rho_{\rm grain}}{3\,{\rm g\,cm^{-3}}} \right) \left(\frac{s_{\rm grain}}{1\,{\rm mm}} \right), \quad (2)$$

where $\rho_{\rm grain}$ is the intrinsic grain density and $s_{\rm grain}$ is the grain size. Modelling dust–gas dynamics in discs is usually uncertain because the gas surface density is poorly constrained, being measured only from multiplying the dust continuum emission by a factor (typically 100). For HD 142527 we are already confident in our assumed surface density profile because of our match to the measured gas mass inside the cavity and to the surface density profile (Fig. 3). However, there remains uncertainty in the assumed CO-to-H_2 conversion.

Our assumed gas disc mass of $0.01\,{\rm M}_\odot$ corresponds to $\Sigma = 0.6\,{\rm g\,cm^{-2}}$ at $R = R_{\rm in}$, giving a Stokes number for mm grains of ≈0.3 at 90 au and ≈1 at 300 au (see Fig. 3). Thus we expect decoupling of grains in the outer disc, since $S_{\rm t} = 1$ corresponds to maximal radial drift (Weidenschilling 1977).

Since orbit R2 produces a cavity close to the observed size with a prominent asymmetry seen in the gas in the PA similar to the observed mm horseshoe, we computed two additional simulations using grain sizes of 1 mm and 100 μm, respectively. We set up dust disc initially between $R_{\rm in} = 120$ au and $R_{\rm out} = 250$ au using 2.5×10^4 dust particles, with an (arbitrary) initial dust-to-gas ratio of 0.01 and properties otherwise reflecting the gas disc (composed of the usual 10^6 SPH particles). The smaller dust disc is merely to avoid numerical problems during the initial disc response to the binary. This also ensures that any dust migration to the cavity edge occurs naturally rather than as a result of the initial conditions.

Fig. 7 shows the dust column density in these two simulations (left and right, respectively), shown after 62 and 63 binary orbits, respectively, such that the orbital phase of both the binary and the dust structures is consistent with the observations. We find that the

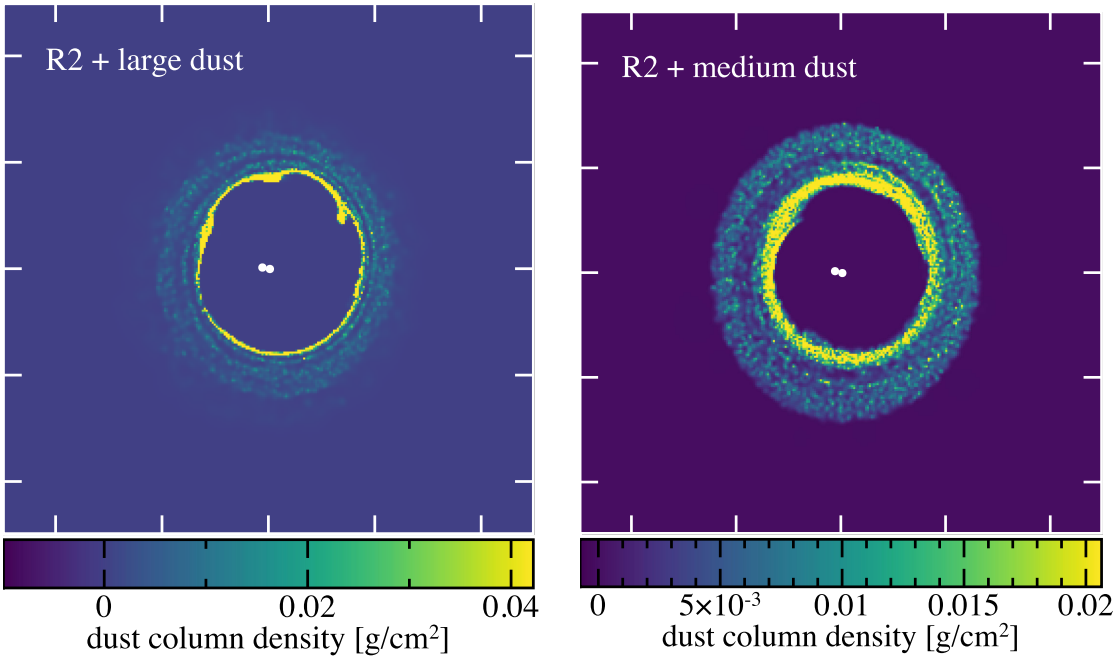

Figure 7. *Dust*. Dust column density in dust–gas simulations using orbit R2 with mm grains (left-hand panel) and 100-μm-sized grains (right-hand panel). Our 'large' (mm) grains are close to Stokes number of unity, and hence quickly migrate to form a thin ring at the cavity edge. Decreasing the grain size by a factor of 10 (right-hand panel) produces a more radially extended dust structure.

dust in both simulations drifts radially, concentrating at the cavity edge within a few tens of orbits. The larger grains, with $S_t \sim 1$, form a thin ring around the cavity edge (left-hand panel). We also observe dust grains collecting into azimuthally distinct structures, trapped by the pressure bumps at the locations where spiral arms in the gas cross the dust ring. Although these grains are nominally 'mm-sized' in our simulations, the resulting dust structures appear more similar to what is seen at cm wavelengths. Fig. 8 shows a direct comparison with the ATCA 34-GHz image from Casassus et al. (2015b) (top left shows the ATCA image; bottom left shows our simulation). To make this comparison we simply convolved our dust column density image to a beam size of 20 au (0.12 arcsec). In hindsight this is not surprising, since the peak emission in wavelength is roughly 2π times the grain size (Kataoka et al. 2016).

Using grains 10 times smaller produces slower migration to the cavity edge and, as a result, a more radially extended dust distribution (right-hand panel of Fig. 7). The asymmetry driven by the binary in the gas produces a horseshoe remarkably similar to the observed mm horseshoe. Fig. 8 makes the direct comparison. The predicted continuum emission is shown in red in Fig. 11.

The main disagreement between the simulations and observations concerns the prominent dip seen in the mm-horseshoe at a PA of $\sim 10^\circ$ (top right). Caution is required in making this comparison since our visualization shown in Fig. 8 assumes optically thin dust emission where spectral index variations show that the continuum emission is optically thick (Casassus et al. 2015b). Our models also do not account for any azimuthal variation in temperature. This is interesting, because a temperature decrement is indeed observed at this PA caused by the shadow from the circumprimary disc. Such a temperature decrement will affect the dust emission and would need to be accounted for in making accurate radiative transfer predictions from our simulations. Moreover, it suggests that thermodynamic effects from the shadow may be important (see Montesinos et al. 2016).

Two conclusions stand out: (i) decoupled dust dynamics around a binary-carved cavity can naturally explain the observed asymmetries in HD 142527 without recourse to vortices or additional companions; and (ii) the distinct 'blobs' seen in the radio emission may be real and not just artefacts of noisy observations.

4.6 Gas density contrast

Casassus et al. (2015b) note that some of the asymmetry seen in the dust emission is also seen in the gas. To quantify this, Fig. 9 compares the predicted ^{13}CO J = 3–2 and C^{18}O J = 3–2 (moment 0) emission maps from simulation R2 (bottom row) to the ALMA observations recently published by Boehler et al. (2017) (top row; see also Muto et al. 2015). For both spectral lines we find a bright, asymmetric ring of emission surrounding the cavity at a radius between 0.5 and 1 arcsec from the central source, as seen in the observations.

The main source of disagreement is that we do not reproduce the two dips in emission at the PAs coincident with the scattered light shadows. This again suggests that the shadowing of the outer disc by the circumprimary disc needs to be accounted for in the CO emission. Our models suggest that the underlying gas density structure is more axisymmetric. If one neglects the dips caused by the shadows, then the contrast in emission around the cavity is similar between our simulations and the observations (i.e. roughly a factor of 2).

Again, the close match with the observed line emission does not suggest alternative hypotheses other than the binary are needed.

4.7 Fast radial flows

Can the streamers seen in Fig. 2 explain the fast radial flows? Fig. 10 shows the radial velocity of the SPH particles, binned as a function of radial distance from the centre of mass (red line), compared to the

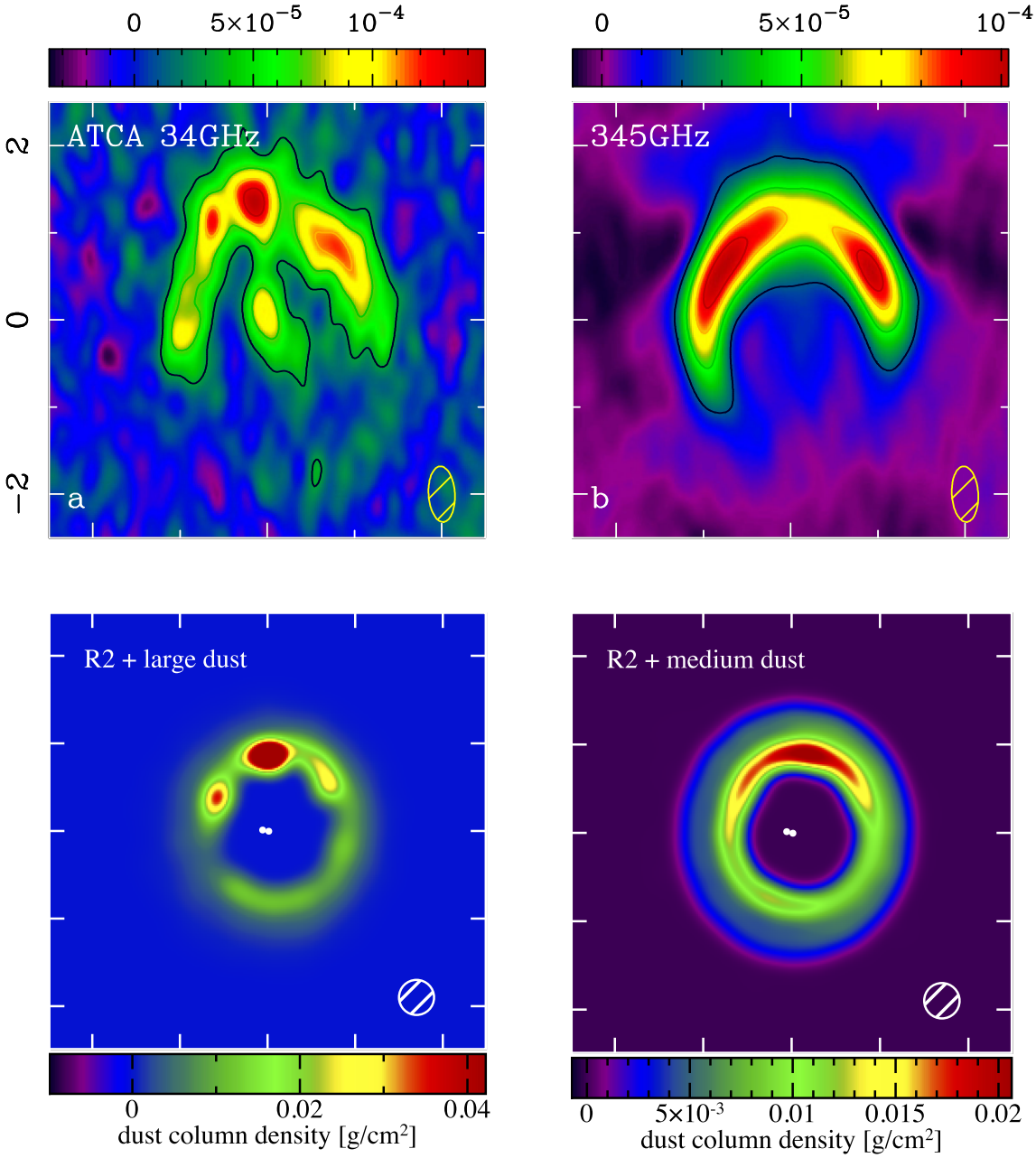

Figure 8. *Horseshoe*. Dust column density comparing observations (top) to our simulations (bottom). We show orbit R2 with grain sizes of 1 mm ('large') and 100 μm ('medium') (bottom panels, left and right, respectively) smeared to a beam size of 20 au (white circle). The larger grains (bottom left) show dust column densities consistent with the ATCA observations at cm wavelengths, while the smaller grains (bottom right) produce an overdense 'horseshoe' in the dust surface density at the correct PA to explain the ALMA observations (top right). Top row credit: fig. 6 of Casassus et al. (2015b) ©AAS, reproduced with permission.

model used to fit the kinematic data by Casassus et al. (2015b) (blue line). Inflow speeds can be seen to reach 10 km s^{-1} at a distance of 20–30 au, consistent with the 'fast radial flows' needed to fit the kinematic data. This suggests that these flows indeed originate in the streams of material that feed the inner disc.

4.8 Gap-crossing filaments

One of the great mysteries in HD 142527 concerns the origin of the 'filaments' of gas seen across the cavity in HCO+ emission by Casassus et al. (2013). These were seen only in HCO+ emission in a particular range of velocity channels. Fig. 11 compares the predicted HCO+ J = 4–3 emission from our simulations (right-hand panel) to the corresponding figure from Casassus et al. (2015a) (left-hand panel). As in the observational figure, we show our predicted continuum map for the mm grains (extrapolated from our 'medium grains' dust simulation) in red, with the predicted HCO+ emission in selected velocity channels in green and the predicted ^{12}CO emission in blue.

Our predicted HCO+ emission shows a thin, faint filament crossing the cavity (right-hand panel), remarkably similar to what is observed (left-hand panel). This suggests that this feature is indeed of

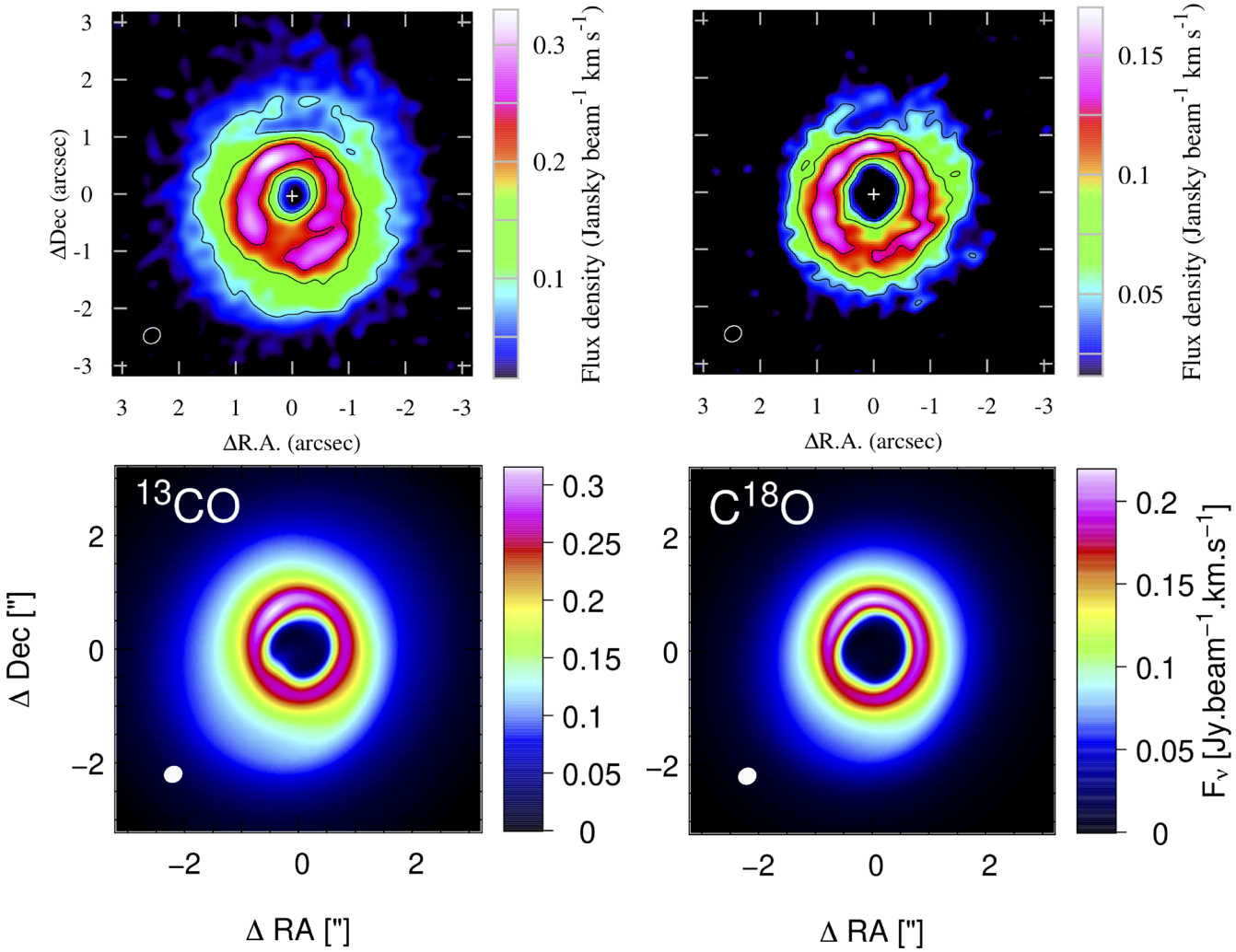

Figure 9. *Gas*. Predicted ^{13}CO J = 3–2 and C^{18}O J = 3–2 emission (moment 0) from simulation R2 after 50 orbits (bottom two panels), compared to Boehler et al. (2017) ALMA data (top two panels; credit: fig. 1 of Boehler et al. 2017 ©AAS, reproduced with permission). The ring-like feature seen in both spectral lines is reproduced in our simulations. The 'broken ring' effect seen in the observations is not reproduced in our models because we do not account for the temperature dip caused by the shadows from the circumprimary disc.

physical origin, originating in the streams of material that feed the circumprimary disc across the cavity. This serves as further confirmation that the dynamical interaction with the binary companion is the source of almost all of the mysterious features present in HD 142527. It also suggests that HCO+ should be more widely employed to detect intracavity flows in circumbinary discs. The main discrepancy our comparison with observations in Fig. 11 is that the PA of the stream differs from our simulation. This mainly indicates that orbit R2 is not the true orbit.

4.9 Kinematics

Finally, Fig. 12 compares the predicted moment 1 maps from simulation R2 in ^{13}CO and C^{18}O emission (bottom row) with the equivalent maps taken from Boehler et al. (2017) using ALMA data (top; see also Muto et al. 2015). Although the broad pattern is similar, there is a small discrepancy between the inner disc kinematics in the observations (top) compared to our simulations (bottom). We attribute this to the secular change in the disc orientation caused by the torque from the binary. This occurs because orbit R2 is not a stable binary–disc configuration. In particular, the torque from the binary on the outer disc vanishes only when the binary is either planar or perpendicular to the disc. It may therefore be fruitful in future investigations to search for orbits that match the observed data but are consistent with one of these arrangements (see discussion below).

5 DISCUSSION

If the observed companion can explain the otherwise unexplained features observed in HD 142527 disc, this has potential implications for our understanding of mm-bright transition discs in general (cf. Casassus 2016; Owen 2016). These represent the fraction of transition discs with large, mm-bright cavities and high mass accretion rates. Observations of transition discs with mass flow on to the central star continuing unabated despite the presence of a large cavity already led numerous authors to conclude that the transition disc population is not a homogeneous class (Alexander & Armitage 2007; Najita, Strom & Muzerolle 2007; Owen & Clarke 2012) and that the likely explanation for the mm-bright subclass is the presence of 'objects massive enough to alter the accretion flow' (Najita,

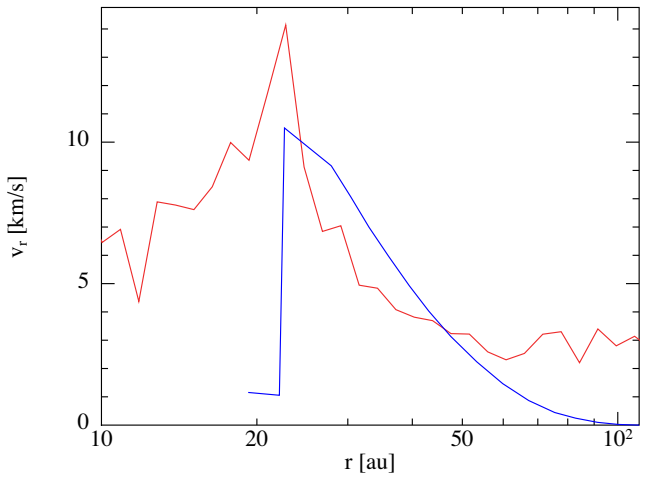

Figure 10. *Fast radial flows*. Maximum inflow velocity on the SPH particles binned as a function of radius, in our model R2 (red), compared to the radial velocity model used to fit the kinematic data (from Casassus et al. 2015b; solid blue line). Fast radial flows of order 10 km s^{-1} occur naturally in the models caused by the streamers that penetrate the cavity.

Andrews & Muzerolle 2015). Such an explanation was offered as far back as Skrutskie et al. (1990).

Cavities in transition discs are thought to be explained by either photoevaporation or companions – the latter either by dynamical clearing, similar to gap opening, or by having simply used up the dust to form planets. We have shown that the cavity in HD 142527 can be satisfyingly explained by dynamical interaction with the observed binary companion, hereby reclassifying it as a circumbinary disc. The streams of gas across the cavity provide a natural explanation for the high accretion rate. Indeed, the average accretion rate in circumbinary discs with $H/R \sim 0.05$ is expected to be similar (within a factor of a few) to that in a disc around a single object (e.g. Farris et al. 2014; Ragusa et al. 2016). In our simulations we measure a mass accretion rate of $\approx 10^{-7}$ M$_\odot$ yr^{-1} on to the primary, consistent with observational estimates of $2(\pm 1) \times 10^{-7}$ M$_\odot$ yr^{-1} (Mendigutía et al. 2014).

Interestingly, HD 142527 is not the first transition disc to have been reclassified as circumbinary. Similar reclassifications were made for CoKu Tau/4 (Ireland & Kraus 2008) (inspiring the first part of our title) and CS Cha (Espaillat et al. 2007; Guenther et al. 2007). This is largely due to the difficulty in detecting close-in companions. HD 142527 demonstrates that it is easy to hide even relatively massive companions inside discs, given that the companion in this case is massive (stellar!) but was only discovered in 2012 due to its close proximity to the central star (Biller et al. 2012).

In a recent study, Ragusa et al. (2017) found that circumbinary discs could naturally explain the cavity-edge rings, asymmetries, and horseshoes seen in ALMA images of mm-bright transition discs including HD 135344B, HD 142527, SR 21, DoAr 44, and Lk Hα 330. Stellar mass companions were only required for the largest asymmetries (i.e. in HD 142527). Substellar companions still produce large cavities, but with lumpy rings around the cavity edge, rather than horseshoes. They found that the required companion masses were consistent with the observational upper limits for the above discs, with IRS 48 a possible exception.

There are already tentative detections of central companions in several other cases of discs with large cavities, including HD 100546 (Quanz et al. 2013, 2015; Brittain et al. 2014; Currie et al. 2014, 2015), LkCa 15 (Sallum et al. 2015), and even more intriguingly in MWC 758 (Reggiani et al. 2018). There are strong hints in other cases (e.g. HD 100453; Wagner et al. 2015). It does not require a great leap of imagination to suppose that the observed companions

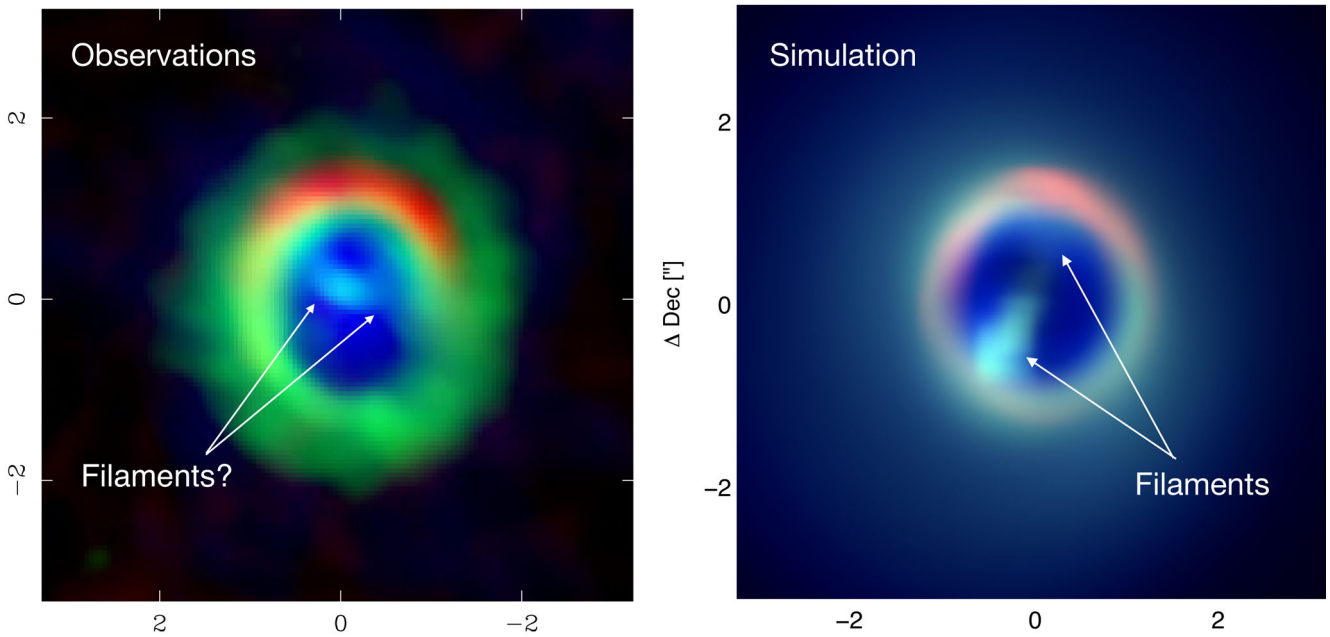

Figure 11. *Streamers*. Predicted HCO+ emission from simulation R2 (right; HCO+ in green), compared to the corresponding Cycle 0 image (left; credit: fig. 8 of Casassus et al. 2015a ©AAS, reproduced with permission). Both images show the mm dust horseshoe in red with HCO+ emission shown in green, with ^{12}CO emission in blue. A filament can be seen crossing the cavity in our simulations, similar to what is observed (albeit with a different PA, indicating our orbit is not the correct one). We thus identify this feature with the streams of material feeding the primary across the circumbinary cavity.

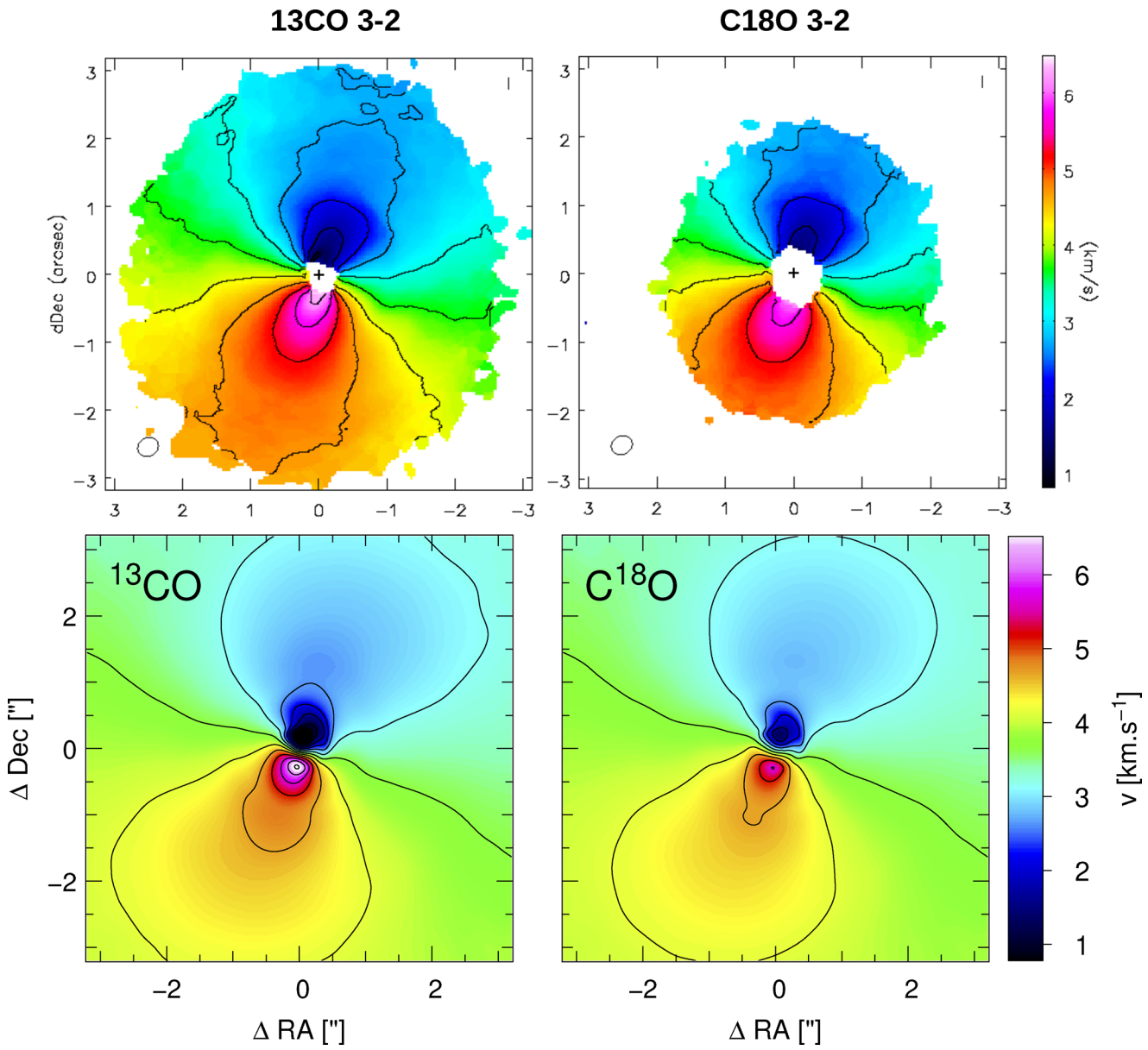

Figure 12. *Kinematics*. Predicted moment 1 emission maps in ^{13}CO 3–2 and C^{18}O from our simulation R2 (bottom left and right, respectively) compared to the observations with ALMA (top; credit: Boehler et al. 2017 ©AAS, reproduced with permission).

may be responsible for the central cavity, spiral arms, and other features in these cases too.

Whether or not our conclusions can be applied beyond the mm-bright subclass is more speculative and beyond the scope of this paper. Certainly stellar mass companions are ruled out in many cases (Pott et al. 2010; Kohn et al. 2016; Ruíz-Rodríguez et al. 2016), nor would they be expected from the known statistics of the field binary population (e.g. Raghavan et al. 2010). Massive planets, however, could perform a similar role in carving central holes in discs, as shown by Ragusa et al. (2017).

No modelling is perfect, and despite some success, there are a number of remaining caveats to our modelling of HD 142527. The main one from our perspective is the secular change in both the binary and outer disc orientation on long time-scales ($\gtrsim$100 orbits). That is, the binary and the disc in our simulations are not in a steady configuration. Recent works by Aly et al. (2015), Martin & Lubow (2017), and Zanazzi & Lai (2018) suggest that the equilibrium configuration for eccentric binaries inclined by more than $\sim$60° is for the disc to align *perpendicular* to the binary (i.e. in a polar alignment). An interesting follow-up would be to try to reproduce the disc features with a binary in such an equilibrium configuration, to see whether it can be ruled in or out (a binary orbit with HD 142527B at 90° to the outer disc seems possible; see L16). An equilibrium configuration is likely given the typical alignment time-scale of order 1000 orbital periods (Martin & Lubow 2017) –10^5 yr in HD 142527 – is much shorter than the disc lifetime ($\sim$Myr). Using better orbital constraints to determine whether the binary is in or out of equilibrium with the disc could therefore place strong constraints on formation models.

A second caveat is the mismatch in the orientation of the streams seen in HCO+ emission. Better orbital constraints should also help to solve this problem, since there are currently a wide range of

possible orbits. The observed orientation of the streamers itself presents a powerful constraint on the orbit.

If large cavities are produced by eccentric massive companions in the disc plane they should be observed, on average, at large projected separations, possibly even embedded in the disc (as appears to be the case in HD 100546). Polar orbits could help to solve this coincidence problem since for a face on disc (such as HD 142527) the range in projected separation on the sky is much smaller. For the orbits we chose for HD 142527, the companion spends 48, 43, and 31 per cent of its period at projected separations less than 20 au (0.13 arcsec) for orbits B1, B2, and B3, respectively. In orbits R1, R2, and R3 this fraction is 19, 22, and 15 per cent, respectively. So the coincidence problem is not too severe with our chosen orbits.

The most valuable observational follow-up would thus be to better constrain the binary orbit and the companion mass, since this directly influences the modelling. Better observations of the inner disc similar to recent observations by Avenhaus et al. (2017) would be very valuable in helping to constrain its geometry, mass, and orientation. Finally, we found that kinematic data provide a rich source of information on the cavity dynamic. In particular, HCO+ is a powerful probe of the streams of gas crossing the cavity. Detection of similar streamers in other mm-bright transitional discs would be a powerful way to infer the presence of hidden companions.

That such eccentric and inclined binaries appear to exist in nature opens many fruitful avenues for theoretical investigation into warped and inclined discs around binaries. For example, Owen & Lai (2017) proposed that large misalignments of inner and outer discs as in HD 142527 may occur through a resonance between the precession period of the inner disc and the precession of the secondary. However, they predict that the orbital plane of the binary should be aligned with the outer disc, which does not appear to be true in HD 142527 based on L16 and our models.

Another interesting direction (in our view) would be to try to infer the binary orbit from the spiral pattern induced around the cavity. This should be possible given sufficient observational constraints on the temperature structure of the disc. Current analytic prescriptions for spiral arms from companions work only in the linear regime (i.e. for low-mass companions; see Ogilvie & Lubow 2002; Rafikov 2002), leading to potentially misleading conclusions regarding the number and mass of the required companions (e.g. Stolker et al. 2016).

The dynamical and thermodynamical influence of the circumprimary disc shadow on the outer disc in HD 142527 also presents an interesting avenue for further investigation. For example, Montesinos et al. (2016) showed that shadows can trigger additional spiral arms in the outer disc.

6 CONCLUSIONS

(i) The cavity, spiral arms, shadows, dust horseshoe, gap-crossing filaments, and fast radial flows seen in HD 142527 can all be explained, in part or in full, by the interaction with the observed central binary companion. HD 142527 should therefore be firmly reclassified as a circumbinary rather than transitional disc.

(ii) Orbits drawn from the best-fitting orbits considered by L16 readily produce a cavity of the required size in HD 142527, implying that the observed binary is likely the origin of the large ≈90 au dust cavity in this disc. Constraints from the cavity size imply a binary semimajor axis $a \lesssim 50$ au.

(iii) Comparison of the spiral structure and shadows with the observations favours the 'red' family of orbits considered by L16 with the binary approaching periastron, with large eccentricity $e = 0.6$–0.7, and almost polar inclination with respect to the outer disc.

(iv) Binary orbits from L16 with the companion approaching periastron naturally produce an inclined circumprimary disc with major axis oriented north–south, fed by streams from the outer disc. This orientation of the inner disc is consistent with the radiative transfer model used by Marino et al. (2015a) to fit the shadows.

(v) We find radial velocities across the cavity of order 10 km s^{-1}, consistent with the observed 'fast radial flows'. We thus offer an explanation for fast radial flows in terms of the streams of material connecting the inner and outer discs.

(vi) We find gas and dust are decoupled in HD 142527. Dust migration to the cavity edge produces features consistent with the observed dust emission, including the prominent mm-horseshoe.

Given that all of the features present in HD 142527 are present in some or all mm-bright transition discs, explaining them may help to explain this class of discs in general. For example, spirals and shadows seen in scattered light around the ∼45 au dust cavity in the disc of HD 135344B (Garufi et al. 2013) are best explained by an 'inner dust ring' inclined by 22° and an 'accretion funnel flow' on to the star (Stolker et al. 2016). In the context of the model we have presented in this paper, these phrases sound eerily familiar.

ACKNOWLEDGEMENTS

This project was initiated during the workshop on 'Planet Formation in the Era of ALMA and Extreme AO' in Santiago, Chile. Section 2 documents a lengthy discussion between many of us while sharing a sushi lunch. DJP thanks S. Casassus, J. Cuadra, Universidad de Chile, Pontificia Universidad Católica de Chile, and the Millenium Nucleus for their hospitality and financial support during two visits to Santiago. We also thank Yann Boehler, Diego Muñoz, Rebecca Martin, and Rebecca Nealon for useful discussions. DJP is funded by an Australian Research Council Future Fellowship FT13010034 and Discovery Projects DP130102078 and DP180104235. We acknowledge CPU time on Gstar/SwinStar at Swinburne University, funded by the Australian Government, and on the MonARCH cluster at Monash. NC acknowledges financial support from FONDECYT grant 3170680. JC and NC acknowledge Millenium Nucleus grant RC130007 (Chilean Ministry of Economy). GMK is supported by the Royal Society as a University Research Fellow. JC acknowledges support from CONICYT-Chile through FONDECYT (1141175) and Basal (PFB0609) grants. We thank the anonymous referee for comments that have improved the paper.

REFERENCES

Alexander R. D., Armitage P. J., 2007, MNRAS, 375, 500
Aly H., Dehnen W., Nixon C., King A., 2015, MNRAS, 449, 65
Andrews S. M., Wilner D. J., Espaillat C., Hughes A. M., Dullemond C. P., McClure M. K., Qi C., Brown J. M., 2011, ApJ, 732, 42
Artymowicz P., Lubow S. H., 1994, ApJ, 421, 651
Ataiee S., Pinilla P., Zsom A., Dullemond C. P., Dominik C., Ghanbari J., 2013, A&A, 553, L3
Avenhaus H., Quanz S. P., Schmid H. M., Meyer M. R., Garufi A., Wolf S., Dominik C., 2014, ApJ, 781, 87
Avenhaus H. et al., 2017, AJ, 154, 33
Baruteau C., Zhu Z., 2016, MNRAS, 458, 3927
Bate M. R., Bonnell I. A., Price N. M., 1995, MNRAS, 277, 362
Benisty M. et al., 2015, A&A, 578, L6
Benisty M. et al., 2017, A&A, 597, A42
Biller B. et al., 2012, ApJ, 753, L38

Boehler Y., Weaver E., Isella A., Ricci L., Grady C., Carpenter J., Perez L., 2017, ApJ, 840, 60
Brittain S. D., Carr J. S., Najita J. R., Quanz S. P., Meyer M. R., 2014, ApJ, 791, 136
Bryden G., Chen X., Lin D. N. C., Nelson R. P., Papaloizou J. C. B., 1999, ApJ, 514, 344
Canovas H., Ménard F., Hales A., Jordán A., Schreiber M. R., Casassus S., Gledhill T. M., Pinte C., 2013, A&A, 556, A123
Canovas H., Caceres C., Schreiber M. R., Hardy A., Cieza L., Ménard F., Hales A., 2016, MNRAS, 458, L29
Casassus S., 2016, Publ. Astron. Soc. Aust., 33, e013
Casassus S., Perez M. S., Jordán A., Ménard F., Cuadra J., Schreiber M. R., Hales A. S., Ercolano B., 2012, ApJ, 754, L31
Casassus S. et al., 2013, Nature, 493, 191
Casassus S. et al., 2015a, ApJ, 811, 92
Casassus S. et al., 2015b, ApJ, 812, 126
Christiaens V., Casassus S., Perez S., van der Plas G., Ménard F., 2014, ApJ, 785, L12
Christiaens V. et al., 2018, A&A, submitted
Close L. M. et al., 2014, ApJ, 781, L30
Cuadra J., 2016, in Resolving Planet Formation in the Era of ALMA and Extreme AO. ESO/NRAO Workshop, Santiago, Chile, id. 30 doi:10.5281/zenodo.58297
Currie T. et al., 2014, ApJ, 796, L30
Currie T., Cloutier R., Brittain S., Grady C., Burrows A., Muto T., Kenyon S. J., Kuchner M. J., 2015, ApJ, 814, L27
Dipierro G., Pinilla P., Lodato G., Testi L., 2015a, MNRAS, 451, 5493
Dipierro G., Price D., Laibe G., Hirsh K., Cerioli A., Lodato G., 2015b, MNRAS, 453, L73
Dipierro G., Laibe G., Price D. J., Lodato G., 2016, MNRAS, 459, L1
Dong R., Zhu Z., Rafikov R. R., Stone J. M., 2015, ApJ, 809, L5
D'Orazio D. J., Haiman Z., Duffell P., MacFadyen A., Farris B., 2016, MNRAS, 459, 2379
Draine B. T., 2003, ApJ, 598, 1017
Dunhill A. C., Cuadra J., Dougados C., 2015, MNRAS, 448, 3545
Espaillat C., Calvet N., D'Alessio P., Hernández J., Qi C., Hartmann L., Furlan E., Watson D. M., 2007, ApJ, 670, L135
Espaillat C. et al., 2014, in Beuther H., Klessen R. S., Dullemond C. P., Henning T., eds, Protostars and Planets VI. Univ. Arizona Press, Tucson, AZ, p. 497
Facchini S., Lodato G., Price D. J., 2013, MNRAS, 433, 2142
Farris B. D., Duffell P., MacFadyen A. I., Haiman Z., 2014, ApJ, 783, 134
Fujiwara H. et al., 2006, ApJ, 644, L133
Fukagawa M., Tamura M., Itoh Y., Kudo T., Imaeda Y., Oasa Y., Hayashi S. S., Hayashi M., 2006, ApJ, 636, L153
Gaia C ollaboration et al., 2016, A&A, 595, A2
Garcia Lopez R., Natta A., Testi L., Habart E., 2006, A&A, 459, 837
Garufi A. et al., 2013, A&A, 560, A105
Guenther E. W., Esposito M., Mundt R., Covino E., Alcalá J. M., Cusano F., Stecklum B., 2007, A&A, 467, 1147
Ireland M. J., Kraus A. L., 2008, ApJ, 678, L59
Kataoka A. et al., 2016, ApJL, 831, L12
Kley W., Dirksen G., 2006, A&A, 447, 369
Kohn S. A., Shkolnik E. L., Weinberger A. J., Carlberg J. K., Llama J., 2016, ApJ, 820, 2
Lacour S. et al., 2016, A&A, 590, A90 (L16)
Laibe G., Price D. J., 2012a, MNRAS, 420, 2345
Laibe G., Price D. J., 2012b, MNRAS, 420, 2365
Lodato G., Price D. J., 2010, MNRAS, 405, 1212
Lubow S. H., D'Angelo G., 2006, ApJ, 641, 526
Lyra W., Lin M.-K., 2013, ApJ, 775, 17
Marino S., Perez S., Casassus S., 2015a, ApJ, 798, L44
Marino S., Casassus S., Perez S., Lyra W., Roman P. E., Avenhaus H., Wright C. M., Maddison S. T., 2015b, ApJ, 813, 76
Martin R. G., Lubow S. H., 2017, ApJ, 835, L28
Mendigutía I., Fairlamb J., Montesinos B., Oudmaijer R. D., Najita J. R., Brittain S. D., van den Ancker M. E., 2014, ApJ, 790, 21
Min M., Stolker T., Dominik C., Benisty M., 2017, A&A, 604, L10
Miranda R., Lai D., 2015, MNRAS, 452, 2396
Monaghan J. J., 2005, Rep. Progress Phys., 68, 1703
Montesinos M., Perez S., Casassus S., Marino S., Cuadra J., Christiaens V., 2016, ApJ, 823, L8
Muñoz D. J., Lai D., 2016, ApJ, 827, 43
Muto T. et al., 2015, PASJ, 67, 122
Najita J. R., Strom S. E., Muzerolle J., 2007, MNRAS, 378, 369
Najita J. R., Andrews S. M., Muzerolle J., 2015, MNRAS, 450, 3559
Nealon R., Price D. J., Nixon C. J., 2015, MNRAS, 448, 1526
Nixon C., King A., Price D., 2013, MNRAS, 434, 1946
Ogilvie G. I., Lubow S. H., 2002, MNRAS, 330, 950
Ohashi N., 2008, Ap&SS, 313, 101
Owen J. E., 2016, Publ. Astron. Soc. Aust., 33, e005
Owen J. E., Clarke C. J., 2012, MNRAS, 426, L96
Owen J. E., Lai D., 2017, MNRAS, 469, 2834
Pearce T. D., Wyatt M. C., Kennedy G. M., 2015, MNRAS, 448, 3679
Perez S. et al., 2015, ApJ, 798, 85
Pérez L. M. et al., 2016, Science, 353, 1519
Pinilla P., Birnstiel T., Ricci L., Dullemond C. P., Uribe A. L., Testi L., Natta A., 2012, A&A, 538, A114
Pinte C., Ménard F., Duchêne G., Bastien P., 2006, A&A, 459, 797
Pinte C., Harries T. J., Min M., Watson A. M., Dullemond C. P., Woitke P., Ménard F., Durán-Rojas M. C., 2009, A&A, 498, 967
Pohl A., Pinilla P., Benisty M., Ataiee S., Juhász A., Dullemond C. P., Van Boekel R., Henning T., 2015, MNRAS, 453, 1768
Pott J.-U., Perrin M. D., Furlan E., Ghez A. M., Herbst T. M., Metchev S., 2010, ApJ, 710, 265
Price D. J., 2012, J. Comput. Phys., 231, 759
Price D. J. et al., 2018, preprint (arXiv:1702.03930)
Quanz S. P., Amara A., Meyer M. R., Kenworthy M. A., Kasper M., Girard J. H., 2013, ApJ, 766, L1
Quanz S. P., Amara A., Meyer M. R., Girard J. H., Kenworthy M. A., Kasper M., 2015, ApJ, 807, 64
Quillen A. C., 2006, ApJ, 640, 1078
Rafikov R. R., 2002, ApJ, 572, 566
Raghavan D. et al., 2010, ApJS, 190, 1
Ragusa E., Lodato G., Price D. J., 2016, MNRAS, 460, 1243
Ragusa E., Dipierro G., Lodato G., Laibe G., Price D. J., 2017, MNRAS, 464, 1449
Reggiani M. et al., 2018, A&A, 611, A74
Rice W. K. M., Armitage P. J., Wood K., Lodato G., 2006, MNRAS, 373, 1619
Rodigas T. J., Follette K. B., Weinberger A., Close L., Hines D. C., 2014, ApJ, 791, L37
Rosenfeld K. A., Chiang E., Andrews S. M., 2014, ApJ, 782, 62
Ruíz-Rodríguez D., Ireland M., Cieza L., Kraus A., 2016, MNRAS, 463, 3829
Sallum S. et al., 2015, Nature, 527, 342
Siess L., Dufour E., Forestini M., 2000, A&A, 358, 593
Skrutskie M. F., Dutkevitch D., Strom S. E., Edwards S., Strom K. M., Shure M. A., 1990, AJ, 99, 1187
Stolker T. et al., 2016, A&A, 595, A113
Strom K. M., Strom S. E., Edwards S., Cabrit S., Skrutskie M. F., 1989, AJ, 97, 1451
van Boekel R. et al., 2004, Nature, 432, 479
van der Marel N. et al., 2013, Science, 340, 1199
van der Marel N., van Dishoeck E. F., Bruderer S., Andrews S. M., Pontoppidan K. M., Herczeg G. J., van Kempen T., Miotello A., 2016, A&A, 585, A58
Verhoeff A. P. et al., 2011, A&A, 528, A91
Wagner K., Apai D., Kasper M., Robberto M., 2015, ApJ, 813, L2
Weidenschilling S. J., 1977, MNRAS, 180, 57
Williams J. P., Cieza L. A., 2011, ARA&A, 49, 67
Zanazzi J. J., Lai D., 2018, MNRAS, 473, 603
Zhu Z., Nelson R. P., Dong R., Espaillat C., Hartmann L., 2012, ApJ, 755, 6

This paper has been typeset from a TEX/LATEX file prepared by the author.